



Morphological, Structural and Optical Properties of Fe-Doped WO₃ Films Deposited by Spray-Pyrolysis

Elaid Ouadah¹ · Nasr-Eddine Hamdadou¹ · Abdelkader Ammari^{1,2}

Received: 14 February 2021 / Accepted: 18 October 2021 / Published online: 16 November 2021
© The Minerals, Metals & Materials Society 2021

Abstract

The present study reports on the synthesis of Fe-doped tungsten trioxide (WO₃:Fe) thin films using spray-pyrolysis technique. The films were deposited on glass substrates at 350°C and Fe-doping was achieved using granular iron in an acidic medium with $\frac{[Fe]}{[W]} = 1, 3$ and 5 % at. The films were heat-treated with an extended thermal treatment at 400°C and 500°C for 4 h, in order to allow both crystallization and dopant diffusion into the WO₃ matrix. The effect of Fe-doping and heat-treatment on the morphological, structural and optical properties of these films was investigated. The results revealed that Fe-doping has a significant impact on the morphology of the films depending on its concentration. In addition, it was shown that the thermal treatment improves the growth of the crystallites and enhances the roughness of the surface. Grazing incidence X-ray diffraction analysis (GIXRD) confirmed the polycrystalline character of the films with a monoclinic structure (ICDD N° 89-4476, P2₁/c). The structural parameters were found to be both doping- and heat-treatment-dependent. Energy dispersive spectrometry (EDS) depicted homogeneous doping and confirmed the presence of W, O and Fe. The films display a good optical transmittance over the visible region sensitive to Fe-doping and thermal treatment. Moreover, the films exhibit both direct and indirect electronic transitions, where the energy of the indirect electronic allowed transition shows a redshift in all the samples due to Fe-doping. Therefore, the width of the tail states energy increases inferring the influence of disorder and the introduction of defect states within the band gap region.

Keywords WO₃ thin films · spray-pyrolysis · Fe-doping · roughness · tail states

Introduction

In recent years, transparent conducting oxide (TCO) films have attracted the attention of several researchers because of their multiple applications such as gas sensors, solar cells, biosensors and catalysts.¹ Currently, various transition metal oxides, such as TiO₂, SnO₂, ZnO, and CdO, have been widely studied.^{2–4} Tungsten trioxide (WO₃) is an

interesting material due to its electrical conductivity, excellent selectivity and high sensitivity.^{1,5,6} Furthermore, WO₃ is an *n*-type wide band gap semiconductor with an optical gap of 2.5–3.6 eV, which can easily be deposited with a high optical transparency in the visible range. In this respect, WO₃ is a material of choice owing to its attractive physical and chemical properties for many applications such as gas sensors,^{7,8} batteries,⁹ electrochromics^{10,11} and photo- and/or electrocatalysis.^{12–15} Several methods have been used for the synthesis of WO₃ films: thermal evaporation,¹⁶ magnetron sputtering,^{17–19} electron beam evaporation,^{20,21} laser ablation,^{22,23} spray-pyrolysis²⁴ and sol-gel.^{25,26}

Among those methods used for thin films preparation we have chosen spray-pyrolysis for the preparation of WO₃ films in our study because of its simplicity, low cost with high growth rate and easy control of doping. Hence, this technique is an efficient method to deposit films with controllable properties. To improve the physical and chemical properties of WO₃ thin films, several dopants have been used such as Pd, Gd, Co, In, and Zn.^{25,27–30} On the other hand, the

✉ Abdelkader Ammari
ammari.hoss@gmail.com; abdelkader.ammari@univ-tiaret.dz

Elaid Ouadah
ouadahelaid@gmail.com

Nasr-Eddine Hamdadou
nhamdadou@gmail.com

¹ Laboratory of Micro and Nanophysics (LaMiN), National Polytechnic School of Oran (ENPO) Maurice AUDIN, BP 1523 Oran, Algeria

² Department of Physics, Faculty of Matter Sciences, Ibn-Khaldoun University, Tiaret, Algeria

dopant can be easily added to the precursor solution with a certain amount when using the sol-gel method. Commonly, we use metal salts such as hydrated chlorides, sulphates and nitrates. However, these precursors contain Cl⁻, NO₃⁻ and SO₄⁻ anions with an important ratio. These impurities remain in the films with small concentration (even after the post heat-treatment) and influence their properties. In our study, we have chosen the element (Fe) as dopant because of the closeness of the ionic radii of W⁶⁺ compared to Fe³⁺ and due to the remarkable bowing effect of Fe-doping on the band gap of the material. Indeed, Khan et al.³¹ have reported that the electronic state created by Fe³⁺ cations above the valence band could trap and transfer electrons and holes to inhibit the recombination of photo-excited holes and electrons. On the other hand, doping in the sol-gel process is usually achieved using mineral salts such as nitrates. The present study reports on the synthesis and the deposition of Fe-doped WO₃ films with small doping concentrations (1, 3 and 5 at.%), where Fe-doping was achieved using granular iron in an acidic medium. Furthermore, an extended thermal treatment at 400°C and 500°C was used in order to allow the dopant diffusion during crystallization of WO₃ films. To the best of our knowledge, this procedure was not reported previously and it is expected to permit using the dopant directly while minimizing the concentration of the undesirable anions that may influence the properties of the films when compared the procedure used commonly in the sol-gel method.

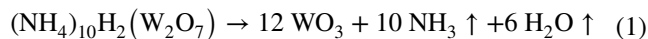
Experimental Details

Thin Film Preparation

WO₃ films were deposited on glass substrates (26 × 10 × 1) mm³ at constant temperature of 350°C by spray-pyrolysis using a Holmarc Spray Pyrolysis system. The glass substrates were cleaned in an ultrasonic bath with acetone and ethanol three times for 5 min then with deionized water to remove traces of microscopic impurities. All the reagents used in the synthesis of the films were purchased from Sigma-Aldrich.

The precursor solution was prepared from ammonium tungstate (NH₄)₁₀H₂(W₂O₇)₆ dissolved in 100 ml of deionized water (0.005 M). Fe-doping was achieved by adding iron powder (purity ≥ 99.99%; particle size < 10 μm) into the previous solution at the appropriate amount ($\frac{[Fe]}{[W]} = 1, 3 \text{ and } 5 \text{ at.}\%$). Hydrochloric acid was added drop-wise to the solution under stirring until the powder was completely dissolved. After that, the solution was sprayed using a syringe-attached sprayer. An air-directed spray stream was used as a carrier gas. The substrate-jet distance and the

spraying speed were 12 cm and 200 μl min⁻¹, respectively. The deposition time was 8 min with an air pressure of 1.5 bar. The contact of the solution with the heated substrates at 350°C allows the thermal decomposition of the precursor solution, thus producing WO₃ films according to the following chemical reaction:



After cooling to room temperature, the films were heat-treated at 400°C and 500°C for 4 h using a MAGMA THERM programmable tubular oven with a heating rate of 10°C min⁻¹. The purpose of this heat treatment is to allow densification and crystallization of the films. Table I depicts the deposition parameters of the films. In addition, the extended thermal treatment is meant to allow dopant diffusion into WO₃ during crystallization.

Characterization Methods

The thickness of the films was measured using a Dektak XT profilometer, which also gives the roughness parameters of the surface. The data processing was carried out by Vision 64 software. The structural properties were obtained by grazing incidence X-ray diffraction (GIXRD) using an INEL Equinox 3000 diffractometer operating in the range of 0–120° with a filtered Cu-K_α radiation (λ = 1.54056 Å). The data processing was performed by Match 3 software. The surface morphology and roughness were examined by atomic force microscopy (AFM, Nanosurf, Flex-Axiom C 3000) in tapping mode. The optical transmittance and absorbance spectra were recorded at room temperature by a dual beam UV-Vis spectrophotometer (Specord 210 Plus) in the range of 300–1100 nm. The surface morphology of the films was analyzed by scanning electron microscopy (SEM, VEGA3-TESCAN) equipped with an energy dispersive spectrometer (EDS).

Table I Deposition parameters of WO₃ thin films

Parameters	Values
Substrate	Glass
Substrate temperature	350°C
Precursor volume	20 ml
Solvent	Deionized water
Dopant	Fe
Spray rate	200 μl/min
Spray nozzle to substrate distance	12 cm
Spray duration	8 min
Heat treatment	400 and 500°C
Heat duration	4 h

Results and Discussion

Film Thickness and Profile Analysis

The surface profilometry is a non-destructive technique and allows studying the film profile. Several parameters are reliable to the roughness of the surface. Table II shows the primary profile (P_p), total profile (P_t) and thickness (e) of $\text{WO}_3\text{:Fe}$ films heat-treated at 400°C and 500°C for 4 h. It is observed that the surface primary and total profiles decrease with Fe-doping when compared to the undoped film and increase with increasing the temperature of heat treatment.

In addition, the other parameters such as the root mean square deviation of the assessed profile (P_q), the skewness of the assessed profile (P_{sk}), the kurtosis of the assessed profile (P_{ku}), which are gathered in Table III. These parameters are often used to get insights on the surface quality. The assessed profile is characterized by three parameters: its maximum height (P_z), its maximum profile peak height (P_p), and its maximum profile valley depth (P_v).

Figure 1 a and b shows the variation of the surface profile parameters with Fe-doping of the films heat-treated at 400°C and 500°C. It is observed that the parameters

P_q , P_z , P_p and P_v decrease with the increase of the dopant concentration for both temperature of thermal treatment. Hence, Fe-doping improves the quality of the surface. In addition, the values of these parameters are relatively lower in the films heat-treated at 500°C. The values of the skewness (P_{sk}) and the kurtosis (P_{ku}) of the assessed profile increases monotonically for the films heat-treated at 500°C, while they seem to be somewhat scattered for the films heat-treated at 400°C. It is evident that thermal treatment at higher temperature improves the growth of the crystallites and enhances the roughness of the surface.

GIXRD Analysis

Grazing incidence X-ray diffraction (GIXRD) was used to determine the structure, crystallographic growth directions, mesh parameters, and average grain size. Figure 2a, b and c shows the X-ray diffraction patterns of $\text{WO}_3\text{:Fe}$ films before and after the heat treatment at 400°C and 500°C. The data show that before heat treatment, the films are amorphous irrespective of the doping concentration (Fig. 2a).

It is observed that the films have a polycrystalline character after heat treatment for 4 h (Fig. 2b and c). All the observed peaks are assigned to the monoclinic structure of WO_3 tungsten trioxide according to the ICDD card

Table II Thickness (e), primary profile (P_p) and total profile (P_t) of $\text{WO}_3\text{:Fe}$ films

Parameters	Heat treatment at 400°C for 4 h			Heat treatment at 500°C for 4 h		
	1%	3%	5%	1%	3%	5%
e (nm)	2879	2226	2352	3484	2798	2402
P_p (nm)	6667.9	3978.6	1228.6	5466.1	4038.8	3918.6
P_t (nm)	7317.1	4158.7	1310.4	5998.7	4326.2	4057.7

Table III Surface profile parameters of $\text{WO}_3\text{:Fe}$ films after heat treatment for 4 h

Parameters	Formulas	Heat treatment at 400°C			Heat treatment at 500°C		
		1%	3%	5%	1%	3%	5%
P_q (nm)	$P_q = \left[\frac{1}{l} \int_0^l Z^2(x) dx \right]^{1/2}$	1016.1	431.7	167.1	1027.6	516.6	411.2
P_{sk}	$P_{sk} = \frac{1}{(P_{qj})^3} \left[\frac{1}{l} \int_0^l Z^3(x) dx \right]$	2.9	6.1	5.2	3.3	3.8	5.9
P_{ku}	$P_{ku} = \frac{1}{(P_{qj})^4} \left[\frac{1}{l} \int_0^l Z^4(x) dx \right]$	12.5	47.0	32.1	14.1	21.4	45.0
P_z (nm)	$P_z = P_p + P_v$	7317.1	4158.7	1310.5	5998.7	4326.3	4057.7
P_v (nm)	$P_v = \frac{1}{CN} \sum_{i=1}^{CN} P_{vi}$	649.2	180.1	81.9	532.6	287.5	139.1
P_c (μm)	$P_c = \frac{1}{m} \sum_{i=1}^m Z_i$	0	0	0	42.5	0.6	65.5
P_{sm} (μm)	$P_{sm} = \frac{1}{m} \sum_{i=1}^m X S_i$	0	0	0	42.5	0.6	65.5

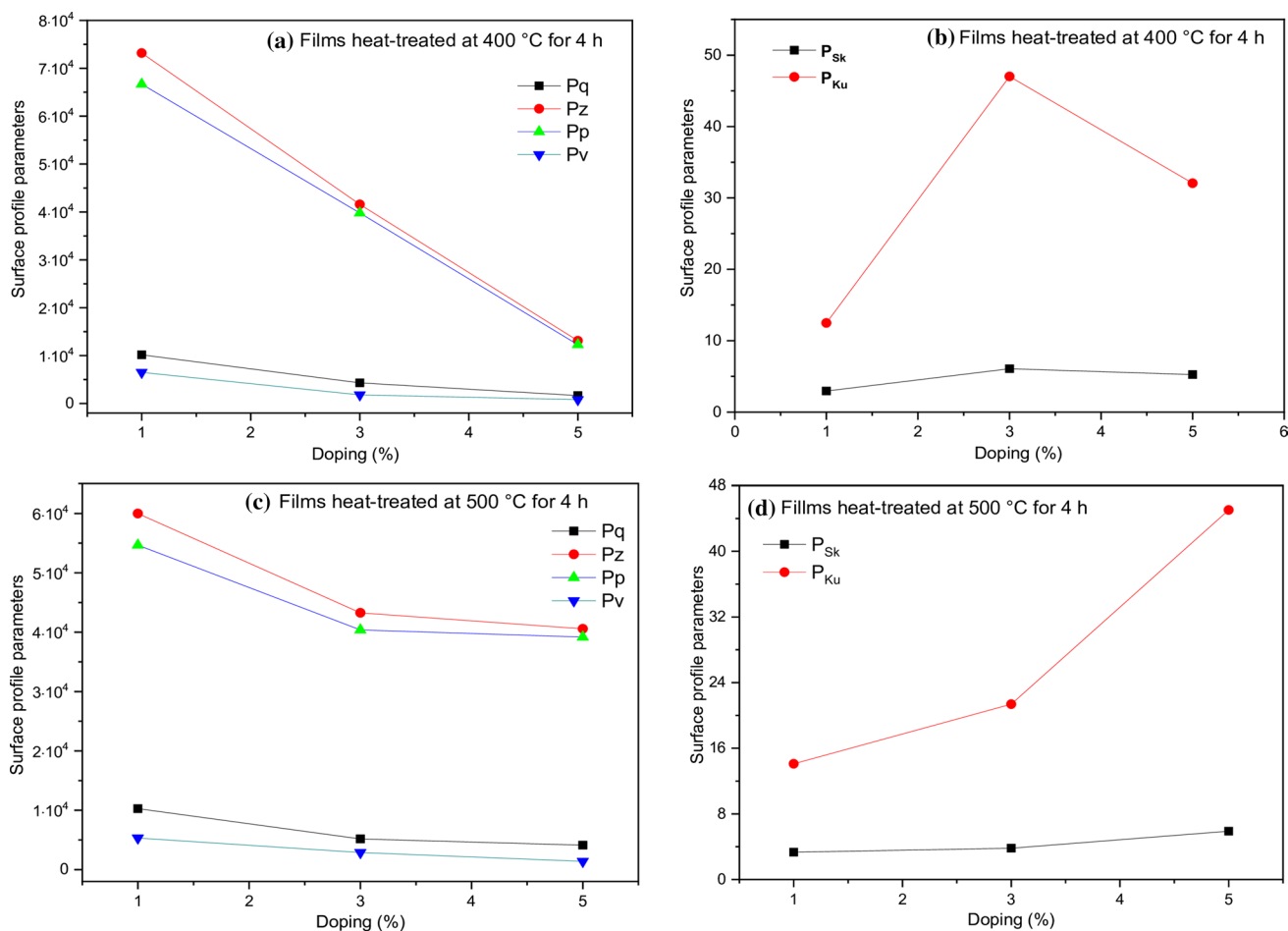


Fig. 1 Surface profile parameters of WO₃:Fe films as a function of doping concentration: (a) the parameters P_q , P_z , P_p and P_v for the films heat-treated at 400°C, (b) the parameters P_{sk} and P_{ku} for the

films heat-treated at 400°C, (c) the parameters P_q , P_z , P_p and P_v for the films heat-treated at 500°C and (d) the parameters P_{sk} and P_{ku} for the films heat-treated at 500°C.

#89-4476. In addition, the patterns confirm the absence of secondary phase related to Fe-doping or crystallization. Table IV shows the Bragg angles (θ), Miller indices (hkl), lattice parameters (a , b , c and β), full width at half maximum (FWHM) of the major intense peak and the average crystallite size (D). All the patterns of the films show at least three well-resolved peaks: (002), (020), (200) and/or ($\bar{1}$ 12). The FWHM of the peaks were calculated using Warren's formula³²:

$$(\text{FWHM})^2 = B^2 - b^2 \quad (2)$$

where B is the experimental widening, which is given directly by the data processing software of the diffractometer, and b is instrumental broadening which is equal to 0.08° in our case. Table IV shows the structural parameters of the films heat-treated at 400°C and 500°C for 4 h. The values of the unit cell parameters are very close to the common values reported in the literature.³³ Particularly, the data reported by

Chang et al.²⁴ using spray coating and Mathankumar et al.²⁷ using simple acid precipitation.

It is observed that the crystallinity of the films was enhanced with the heat treatment. The average crystallite size (D) was determined using Scherrer's formula³⁴:

$$D = 0.9 \frac{\lambda}{\text{FWHM} \cdot \cos \theta} \quad (3)$$

where λ is the X-ray wavelength and FWHM is the real widening of the diffraction peak. The average crystallite size of WO₃:Fe films varies in the range of 13.0–24.7 nm, depending on the temperature of heat treatment and the dopant concentration. It is observed that the crystallite size decreases when compared to that of the undoped film and then increases with increasing concentration of the dopant (3 and 5 at.%). In addition, it is evident that the thermal treatment at 500°C improves the crystal growth,³⁵ and we have observed that the crystallite sizes are bigger when compared to those of the films heat-treated at 400°C. This variation of

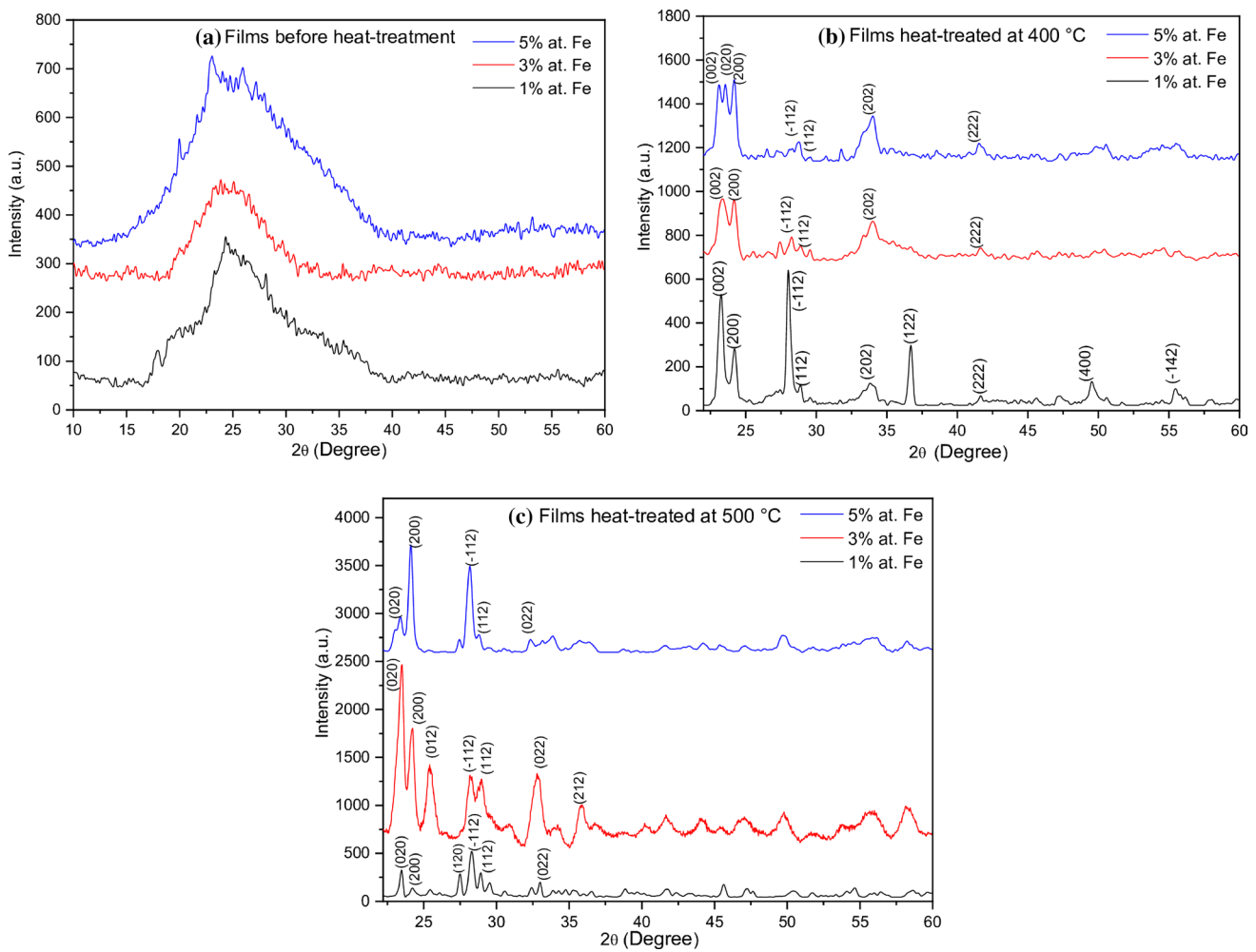


Fig. 2 GIXRD of $\text{WO}_3:\text{Fe}$ films with different doping concentrations: (a) before heat treatment, (b) after heat treatment for 4 h at 400°C , and (c) after heat treatment for 4 h at 500°C .

the crystallite sizes agrees well with the results of both the profile and AFM analysis. Furthermore, substitution of W^{+6} cations (ionic radii: 74 pm) with Fe^{3+} cations (ionic radii: 69 pm) induces a distortion in the crystal lattice and oxygen vacancies (OV) have a tendency to form neighboring these impurities. The increase in OV concentration is considered very advantageous for gas detection.³⁶ The inter-planar distance (d_{hkl}) in the monoclinic system is given by:

$$\begin{cases} \frac{1}{d_{hkl}^2} = \frac{1}{\sin^2 \beta} \left(\frac{h^2}{a^2} + \frac{k^2 \cdot \sin^2 \beta}{b^2} + \frac{l^2}{c^2} - \frac{2 \cdot hk \cdot \cos \beta}{a \cdot b} \right) \\ d_{hkl} = \frac{\lambda}{2 \cdot \sin \theta} \end{cases} \quad (4)$$

Table IV shows that the lattice parameters change with Fe-doping when compared to the undoped film. The unit cell volume decreases and then increases, inferring that the insertion of the dopant occurs dominantly with Fe^{3+} cations occupying the octahedral sites (Scheme 1) for low Fe-doping (1 and 3%) because of the proximity of the ionic

radii. However, it is presumed that the dopant cations are inserted in the interstitial sites for a higher amount of dopant. This behavior is further correlated with the non-stoichiometry of the films for which WO_3 crystal consist of a mixture of $\text{W}^{4+/5+}$ and W^{6+} cations.^{37–39} Therefore, the heterovalent substitution also supports the increase of the unit cell volume for Fe-doping at a higher amount (ca. 5 at.%).

The dislocation density (δ) in the film defines the length of the dislocation lines per crystal volume unit. This density was calculated using the following relation⁴⁰:

$$\delta = \frac{1}{D^2} \quad (5)$$

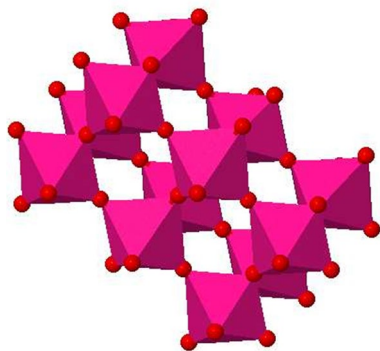
where D is the average crystallite size evaluated from the XRD data. The deformation varies proportionally with the stress (\mathcal{E}), which is the result of the internal forces in matter. The stress (\mathcal{E}) in the studied films was evaluated using the following formula⁴¹:

Table IV Structural parameters of WO₃:Fe films after heat treatment at 400 and 500°C for 4 h

T (°C)	Fe-doping (%)	2θ (°)	(hkl)	Lattice parameters				FWHM (°)	D (nm)	V (Å ³)	ε (× 10 ⁻³)	δ (lines/μm ²)
				a (Å)	b (Å)	c (Å)	β (°)					
400	1%	23.21	(002)	7.3322	7.5644	7.6591	89.13	0.5336	16.3	424.7	2.12	3763.8
		24.26	(200)									
		28.03	($\bar{1}$ 12) ^{MI}									
		33.91	(202)									
	3%	23.35	(002) ^{MI}	7.3496	7.4754	7.6133	90.49	0.6671	13.05	418.3	2.65	5871.9
		24.20	(200)									
		28.22	($\bar{1}$ 12)									
		34.02	(202)									
	5%	23.08	(002)	7.3622	7.5397	7.7017	90.86	0.42684	20.3	427.5	1.69	2402.9
		23.58	(020)									
		24.16	(200) ^{MI}									
		34.02	(202)									
500	1%	23.44	(002)	7.3501	7.6719	7.5880	91.83	0.4278	20.4	427.7	1.70	2426.6
		24.21	(200)									
		28.29	($\bar{1}$ 12) ^{MI}									
		34.02	(202)									
	3%	23.48	(002) ^{MI}	7.3383	7.589	7.5723	90.91	0.58712	14.83	421.6	2.45	4546.9
		24.24	(200)									
		28.21	($\bar{1}$ 12)									
		34.02	(202)									
	5%	23.36	(002)	7.3797	7.6358	7.6100	90.51	0.3523	24.7	428.8	1.40	1639.1
		24.10	(200) ^{MI}									
		28.18	($\bar{1}$ 12)									
		34.02	(202)									

T temperature of thermal treatment, *FWHM* full width at half maximum of the main intense peak, *D* crystallite size, *V* unit cell volume, *ε* lattice strain, *δ* dislocation density

^{MI}major intense peak.



Scheme 1 Crystalline structure of WO₃ with oxygen atoms forming octahedra.

$$\varepsilon = \frac{\beta \cos \theta}{4} \quad (6)$$

where β represents the real widening of the diffraction line and θ the diffraction angle. Table IV shows the results of intrinsic deformations and dislocation density of the films

for both series of samples. It is observed that the stress and the dislocation density increase with increasing dopant concentration from 1% to 3% when compared to the undoped film and then decrease for Fe-doping at 5% regardless of the temperature of thermal treatment, thus indicating the formation of high crystal quality and the reduction of imperfections.^{39,42} In addition, the average crystallite size values are small when compared to the data reported by Luxmi and Kumar⁴³ for the same dopant concentration. On the other hand, they are much greater when compared to those values reported by Ngigi et al.⁴⁴ for the same dopant concentration. By contrast, the values of the stress in our samples are smaller by three orders of magnitude when compared to the data reported by Nguyen et al.⁴⁵ established for nanobrick hybrid WO₃, and they are compared to the values obtained by Thwala and Dlamini⁴⁶ for Mg-doped WO₃ films prepared with a hydrothermal method.

AFM Analysis

Atomic force microscopy (AFM) is an effective technique used to determine the surface morphology and roughness

of films. Figure 3 shows the three-dimensional (3D) surface morphology of Fe-doped WO_3 films heat-treated at 500°C for 4 h.

The average height of the roughness profile (R_c) and the mean square deviation of the roughness profile (R_{rms}) of the surface, were determined using *Nanosurf C3000* software on a surface of $(2 \times 2) \mu\text{m}^2$. The morphological parameters of the films are gathered in Table V.

For all the films, the 3D images show the presence of well-developed grains. The R_{rms} values are 16.9 nm (film doped at 1%), 29.1 nm (film doped at 3%) and 51.0 nm (film doped at 5%), which confirms the enhancement of the roughness of the films. As the doping concentration increases, the average height of the roughness profile (R_c) of the films also increases. The average particle size increases from 104.3 nm (film doped at 1%) to 327.1 nm (film doped at 3%) and 528.4 nm (film doped at 5%) with Fe-doping.

SEM Analysis

Figure 4a, b and c shows the SEM images of Fe-doped WO_3 films heat-treated at 500°C . It is observed that the surface morphology of the films is significantly modified by doping. The film doped at 1% (Fig. 4a) exhibits a porous morphology with spherically shaped small grains on the surface. This particular morphology is highly attractive

Table V Morphological parameters of WO_3 :Fe films after heat treatment at 500°C for 4 h

Fe-doping (%)	R_{RMS} (nm)	D_{aver} (nm)	R_c (nm)
1	16.9	104.3	12.7
3	29.1	327.1	21.9
5	51.0	528.4	42.3

R_{RMS} mean deviation of roughness profile, D_{aver} average grains size, R_c Average height of the roughness profile

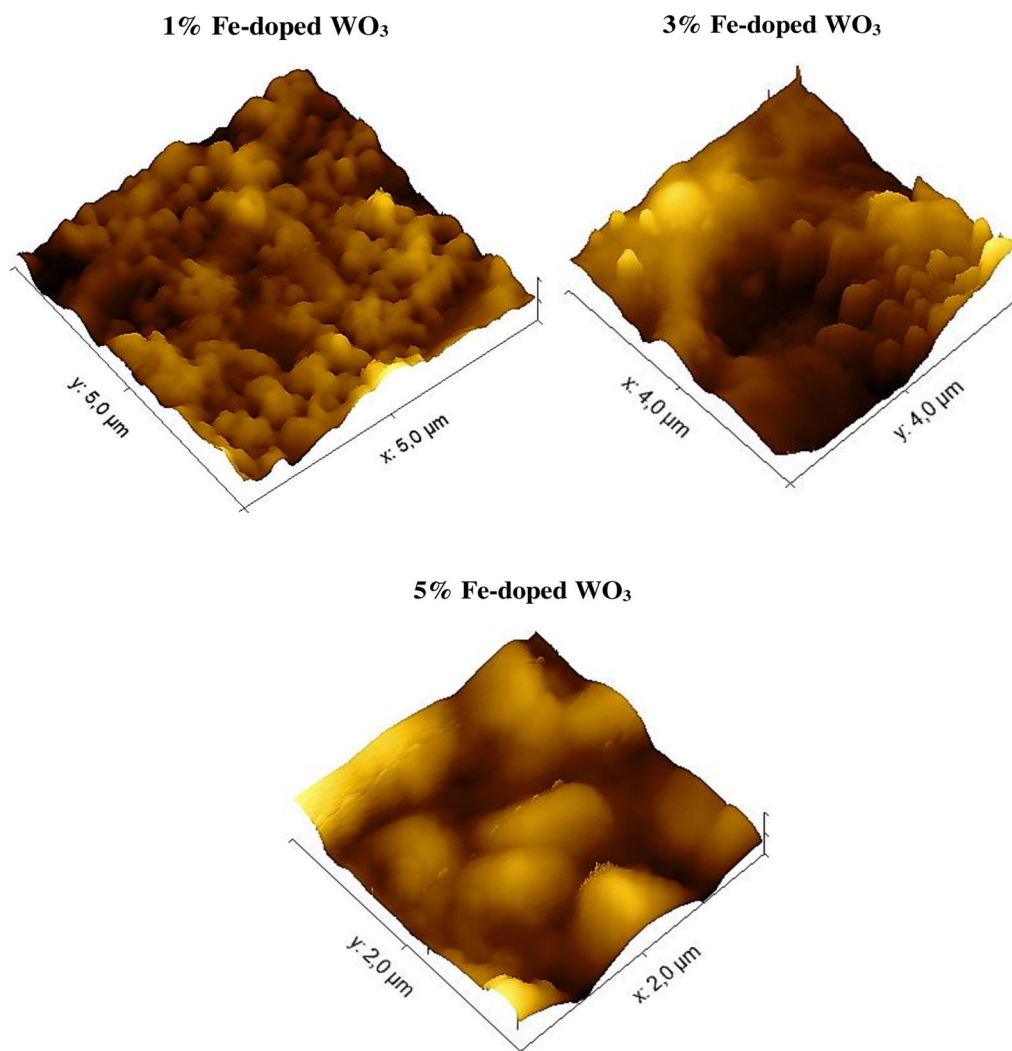


Fig. 3 AFM images of Fe-doped WO_3 films after heat treatment at 500°C for 4 h.

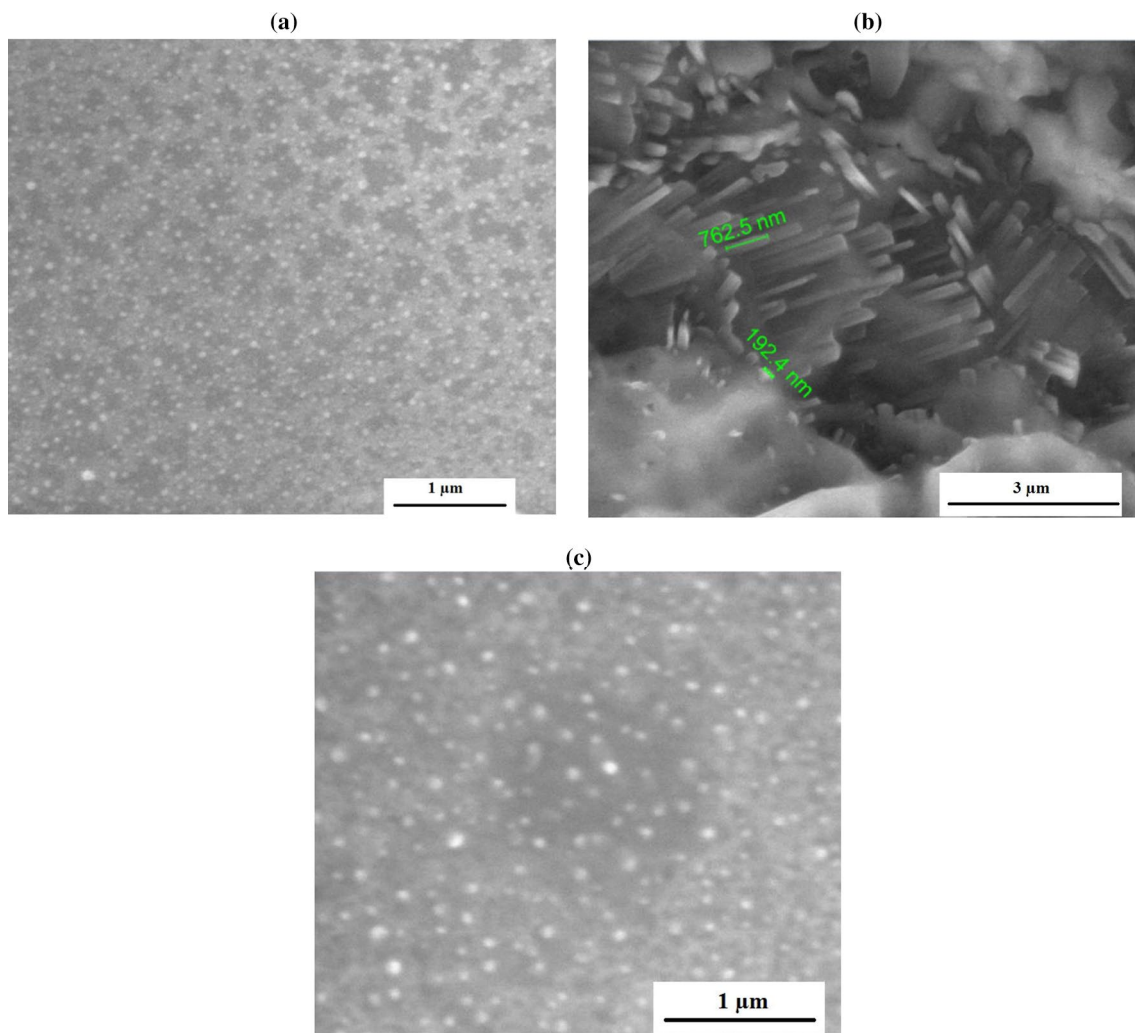


Fig. 4 SEM images of WO₃:Fe films after heat treatment for 4 h at 500°C: (a) film 1% Fe-doped WO₃, (b) film 3% Fe-doped WO₃ and (c) film 5% Fe-doped WO₃.

for gas sensing application.⁴⁷ The regular distribution of these spherical grains is due to the homogeneous substrate temperature and uniform deposition.

On the contrary, the microstructure of film doped at 3% (Fig. 4b) shows differently shaped aggregations, i.e. nanowires of 762 nm length and $\varnothing = 192$ nm, oriented differently and homogeneously dispersed. The surface morphology of the film doped at 5% (Fig. 4c) displays a homogeneous crack-free appearance in all scanned areas with numerous crystallites shaped differently. EDS analysis of the film doped at 5% (Fig. 5) confirmed the presence of W and O and shows that the dopant is homogeneously dispersed in the film. It is evident that Fe-doping has a significant impact on the morphology of the films depending on the concentration.

Finally, the analysis of the structural and morphological data can be summarized as follows:

- We have analyzed the structural properties of three types of samples: amorphous, samples heat-treated at 400°C, and those heat-treated at 500°C. The data showed that the films heat-treated at 500°C have a good crystallinity. Therefore, we have carried out additional analysis on this latter (heat-treated at 500°C) to examine the effect of Fe-doping on their properties.
- The effect of Fe-doping on the structural properties was evidenced by the observed change of the structural parameters (Table V)
- The effect of Fe-doping on the morphology of the sample was evidenced first by observed changes of the profiles parameters (Tables II and III) and then by the observed changes on the SEM micrographs (Fig 4). The results show that the samples exhibits different morphologies depend on the Fe-concentration. Samples doped at both 1% and 3% (Fig. 4a and b) present spherically shaped grains. However, the surface of the film doped at 5%

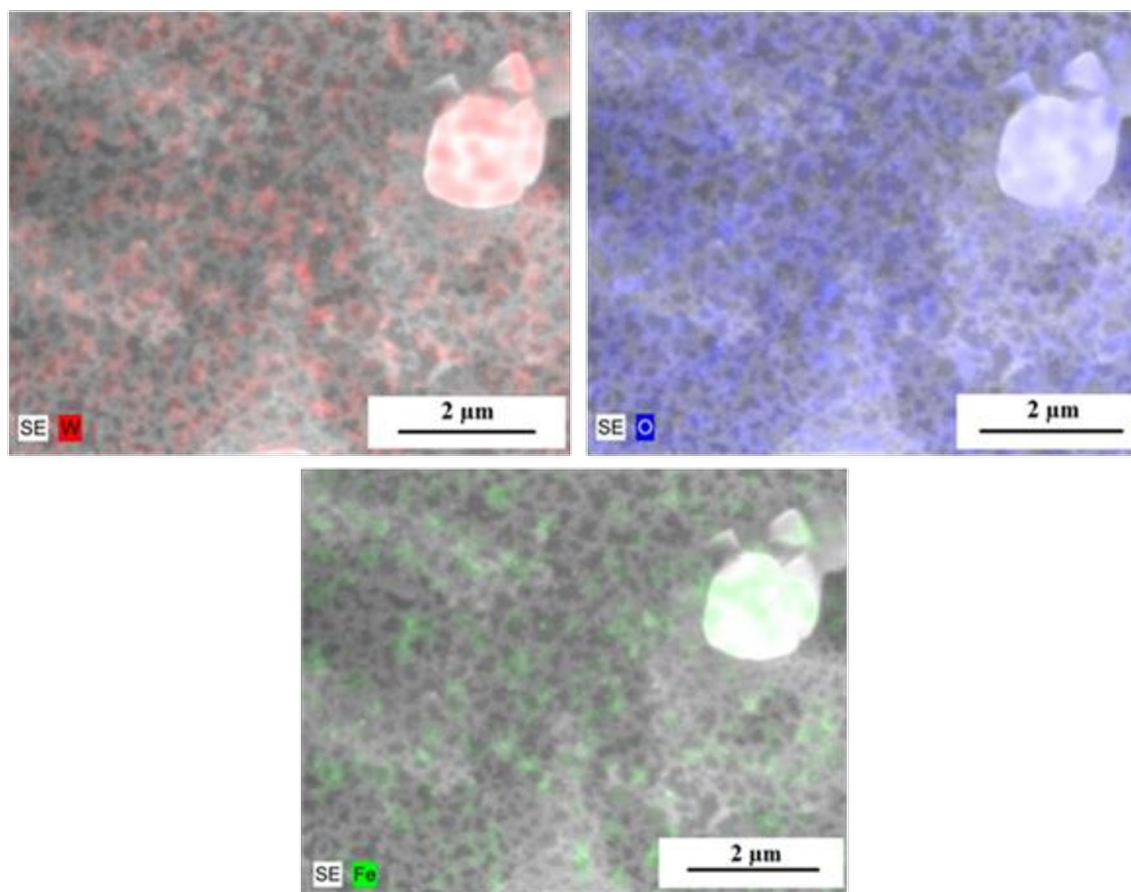


Fig. 5 EDS cartographic analysis of 5% Fe-doped WO_3 film.

appears more homogenous and dense with an average radius relatively greater when compared to that of the film doped at 1 at.%. In addition, the film doped at 3% present a completely different morphology with nanowires of 762 nm length and $\varnothing=192$ nm, oriented differently and homogeneously dispersed.

- The AFM analysis revealed that the roughness parameters increase by 170% after doping at 3% Fe (compared to the film doped at 1% Fe) and increase by more than 300% after doping at 5% Fe. On the other hand, The average grain size increases by more than 300% after doping at 3% Fe (compared to the film doped at 1% Fe) and by more than 500% after doping at 5% Fe.

We have considered the above results to be strong evidence on the changes of the structural and morphological properties induced by Fe-doping.

Optical Analysis

The spectrophotometry performed at room temperature is a non-destructive technique used to determine

the absorbance and the transmittance (T) as a function of the wavelength (λ). Figure 6 shows a sharp decrease of the ultraviolet absorption with increasing wavelength (from 1.4 to 0.17 and 0.12 a.u. for the films heat-treated at 400°C and 500°C, respectively). The average absorbance relatively decreases in the visible range (from 0.17 a.u. to 0.13 a.u. and from 0.12 a.u. to 0.09 a.u. for the films heat-treated at 400°C and 500°C, respectively). The transmittance/absorbance of a film is generally influenced by some factors such as the surface roughness, grain boundary scattering and optical inhomogeneity.⁴⁸

Figure 7 shows that the films have a good optical transmittance in the visible region sensitive to Fe-doping and thermal treatment. Table VI reports the values of the average optical transmittance of the films in the visible range.

Indeed, this variation can be correlated with the thickness, porosity and enhanced scattering effect due to the roughness of the surface.⁴⁹ Particularly, the decrease in the optical transmission is attributed to the propagation losses at the grain boundaries and electronic defects.³⁹

The absorption coefficient (α) was calculated from the transmission spectra using the following formula⁵⁰:

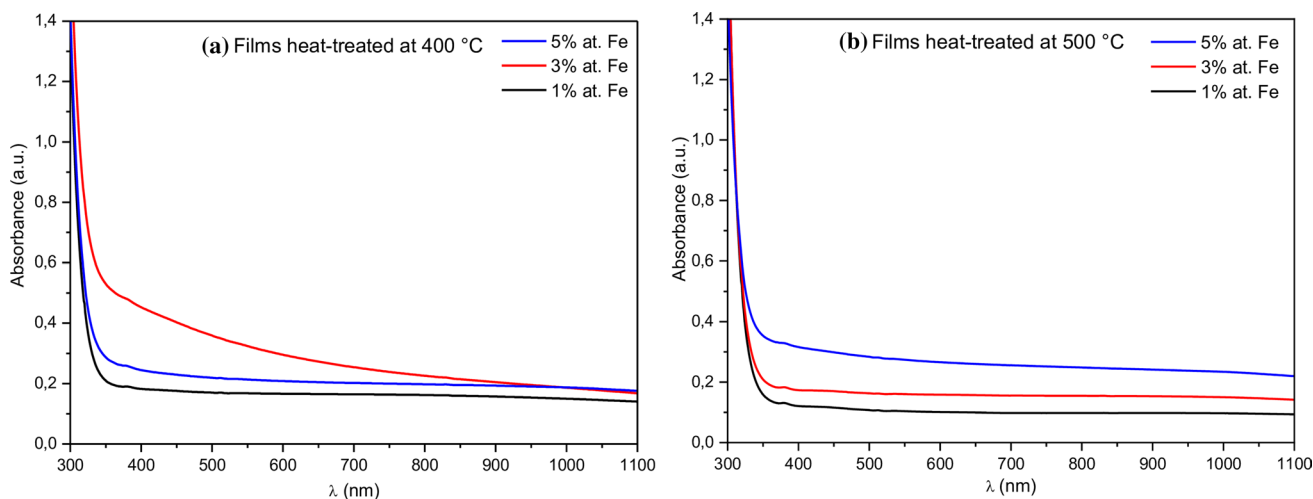


Fig. 6 Absorbance spectra of WO₃:Fe films: (a) films heat-treated for 4 h at 400°C, and (b) films heat-treated for 4 h at 500°C.

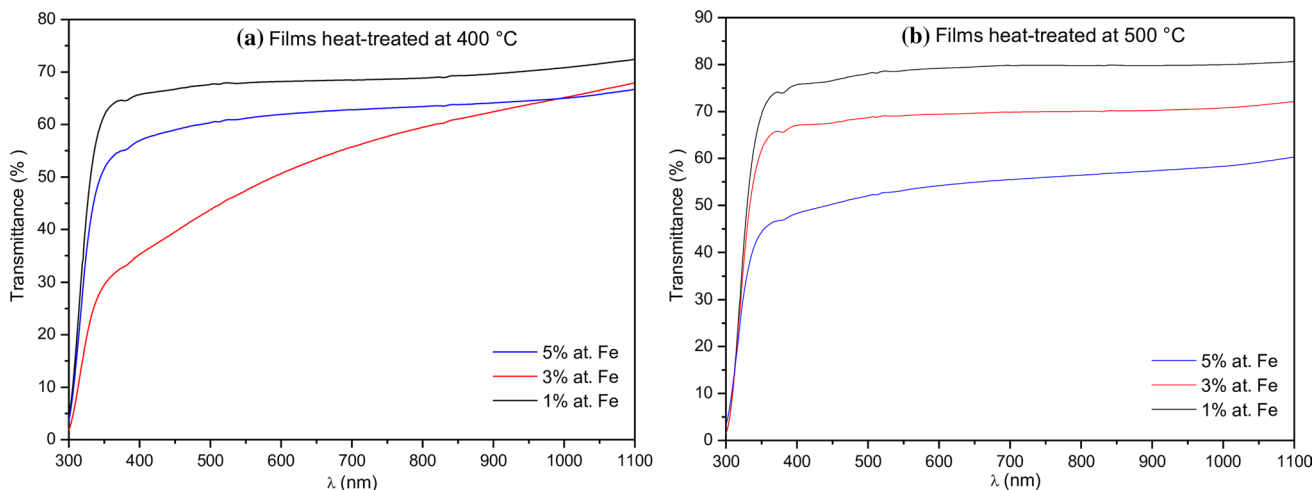


Fig. 7 Transmittance spectra of WO₃:Fe films: (a) films heat-treated for 4 h at 400°C, and (b) films heat-treated for 4 h at 500°C.

Table VI Optical parameters of WO₃:Fe films after heat treatment at 400°C and 500°C for 4 h

T (°C)	Fe-doping (%)	T_{Aver} (%)	E_g^I (eV)	E_g^{II} (eV)	E_u (meV)
400	1	72	4.18	3.83	252
	3	68	4.05	3.68	333
	5	66	4.10	3.76	267
500	1	81	4.22	3.75	217
	3	72	4.18	3.70	237
	5	60	4.13	3.65	276

T temperature of heat treatment, T_{Aver} average optical transmittance, E_g^I direct optical band gap, E_g^{II} indirect optical band gap, E_u Urbach energy

$$\alpha = \frac{1}{e} \ln \left(\frac{100}{T} \right) \quad (7)$$

where e represents the thickness (cm) and T is the optical transmittance (%). Figure 8 shows the variation of the optical absorption coefficient of WO₃:Fe films. The optical absorption coefficient values were reached at low energies $1.27 \times 10^4 \text{ cm}^{-1}$ ($0.84 \times 10^4 \text{ cm}^{-1}$), $1.9 \times 10^4 \text{ cm}^{-1}$ ($1.45 \times 10^4 \text{ cm}^{-1}$) and $2 \times 10^4 \text{ cm}^{-1}$ ($1.72 \times 10^4 \text{ cm}^{-1}$) for 1%, 3% and 5% Fe-doped WO₃ films for the films heat-treated at 400°C (at 500°C, respectively). Furthermore, it is observed that the absorption coefficient increases with Fe-doping for both series of the films.

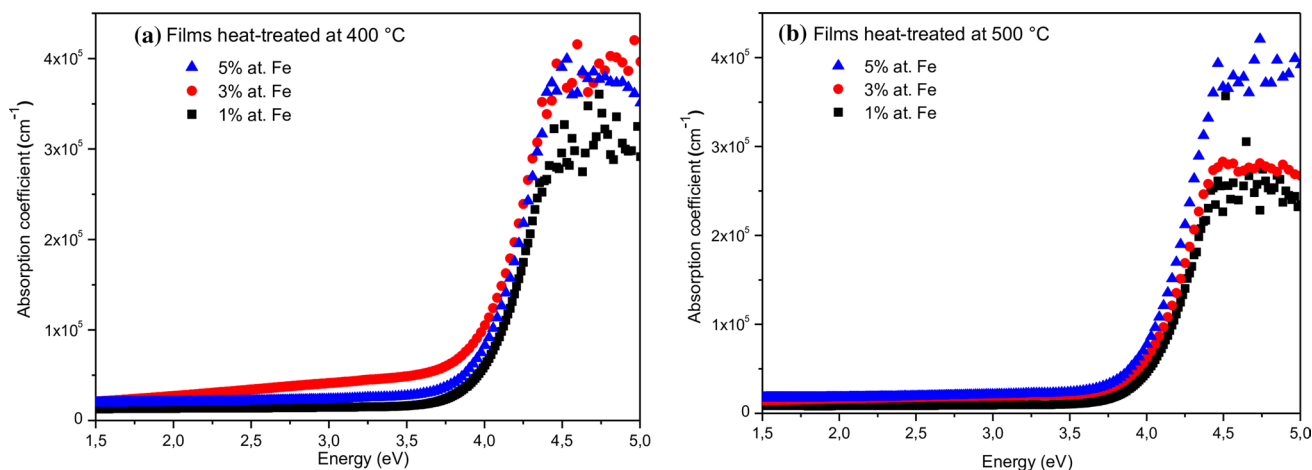


Fig. 8 Variation of the optical absorption coefficients of $\text{WO}_3\text{:Fe}$ films: (a) films heat-treated for 4 h at 400°C , and (b) films heat-treated for 4 h at 500°C .

To determine the energy of the band gap, we have used Tauc's formula, which is given as follows⁵¹:

$$\alpha h\nu = A(h\nu - E_g)^n \quad (8)$$

where A is a constant, h is the Planck constant, ν is the frequency of the incident light. The constant $n = 1/2$ in the case of a direct optical transition and $n = 2$ in the case of an indirect optical transition. E_g is deduced from the plot $(\alpha h\nu)^2$ versus $h\nu$ by linear extrapolation to the abscissa axis (zero absorption).^{52,53} Figure 9a and b shows the plots for indirect and direct allowed optical transitions in the films, respectively. The extrapolation of the linear parts of these curves yields the value of the optical band gap (E_g^I : Direct optical band gap; E_g^{II} : Indirect optical band gap). Table VI shows the obtained values of $\text{WO}_3\text{:Fe}$ films heat-treated at 400°C and 500°C for 4 h. It is observed that E_g^{II} decreases for both series (from 3.83 eV to 3.76 eV for the films heat-treated at 400°C , and from 3.75 eV to 3.65 eV for the films heat-treated at 500°C), while E_g^I decreases only in the films heat-treated at 500°C (from 4.22 eV to 4.13 eV). The decrease of the optical band gap with doping is consistent with the introduction of the impurity levels below the conduction band.⁵⁴ The obtained values of indirect optical band gap (E_g^{II}) are relatively greater when compared to ~ 3.48 eV of WO_3 obtained by inorganic and sol-gel methods.⁵⁵ On the other hand, Eglitis et al. reported using ab initio calculations that the optical transition $\Gamma - \Gamma$ is of 4.95 eV, which is overestimated when compared to our data.⁵⁶ The obtained values of E_g^I for both amorphous and polycrystalline films are close to 3.8 eV reported by Acosta et al.⁵⁷ for Ti doped WO_3 thin films deposited by spray-pyrolysis.

Figure 10a and b shows the semi-logarithmic plots of the absorption coefficient as a function of photon energy. This

region is called the Urbach region. The following relation gives the absorption coefficient⁵⁸:

$$\alpha = \alpha_0 \exp\left(\frac{h\nu}{E_u}\right) \quad (9)$$

Therefore:

$$\ln(\alpha) = \ln(\alpha_0) + \left(\frac{h\nu}{E_u}\right) \quad (10)$$

where α_0 is a constant and E_u is the Urbach energy.

To measure the width of tail states, the Urbach energy (E_u) was calculated from the formula⁵⁹:

$$E_u = \left[\frac{d(\ln\alpha)}{d(h\nu)} \right]^{-1} \quad (11)$$

The Urbach energy values of $\text{WO}_3\text{:Fe}$ films heat-treated for 4 h are gathered in Table VI. Figure 11 shows the variation of the Urbach energy with Fe-doping. It is observed that E_u increases indicating the widening of the tail states.^{58,59} Moreover E_u is sensitive to disorder and the increase of the crystallinity in the films,⁶⁰ which is believed to explain the variation observed for the films heat-treated at 400°C .

Conclusion

Fe-doped WO_3 films were deposited using the reactive chemical spray technique in liquid phase (spray pyrolysis) from an aqueous solution based on ammonium tungstate. From the profile and the morphology analysis, the surface profiles were found to decrease with Fe-doping and

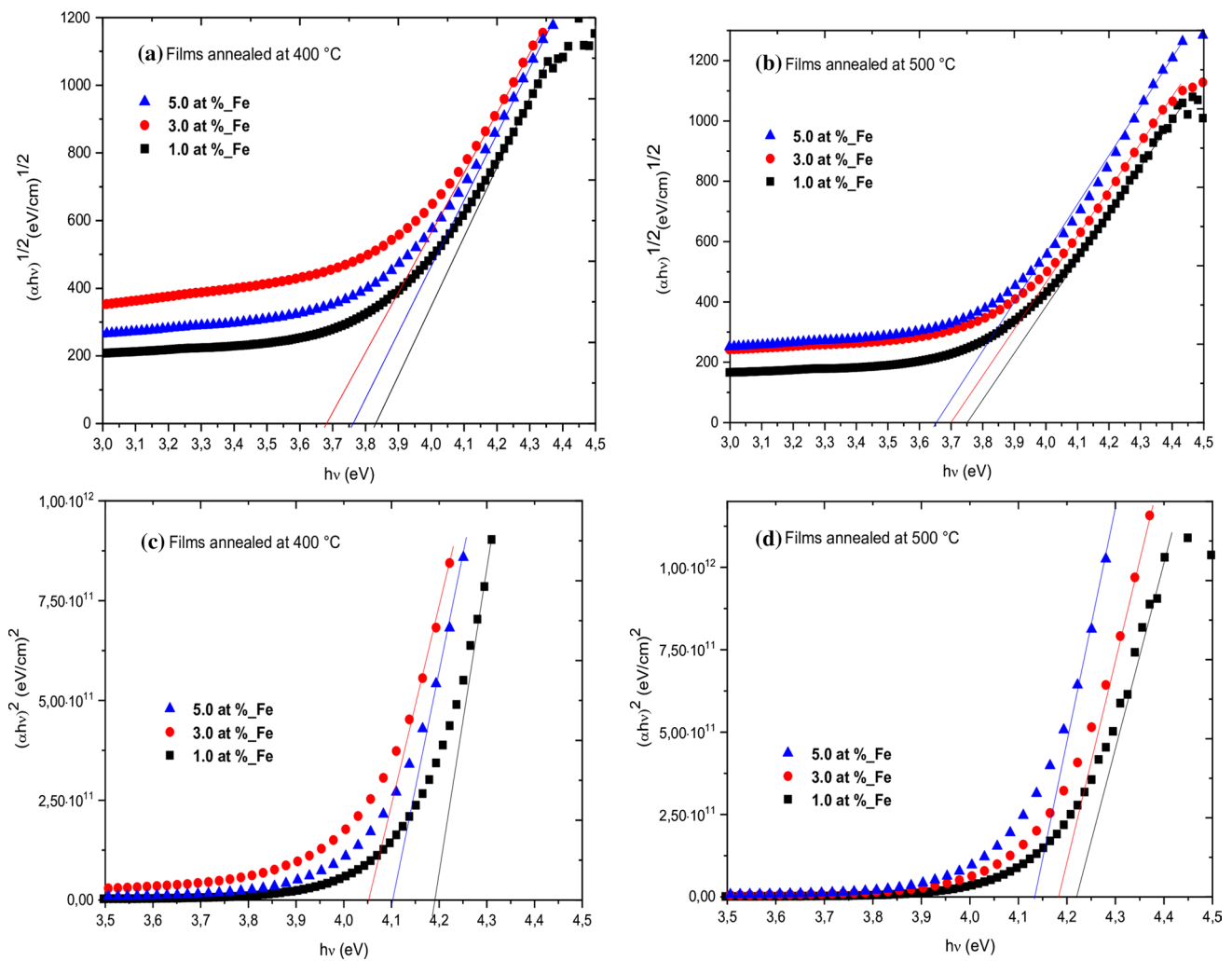


Fig. 9 Optical transitions of WO₃:Fe films: (a) Indirect allowed transitions for the films heat-treated at 400°C, (b) Indirect allowed transitions for the films heat-treated at 500°C, (c) Direct allowed transitions

for the films heat-treated at 500°C and (d) Direct allowed transitions for the films heat-treated at 500°C.

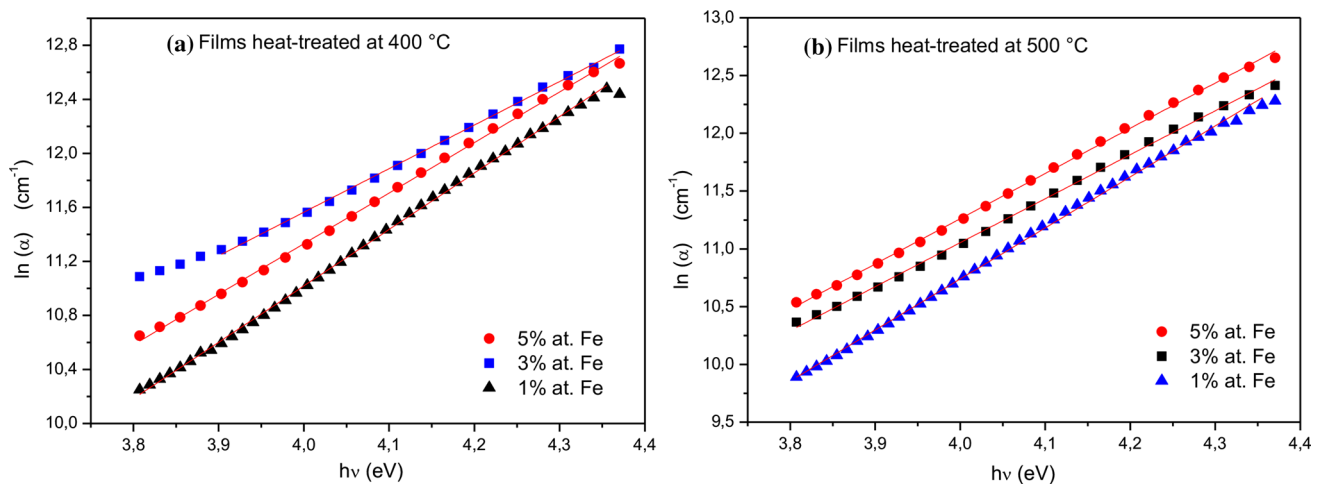


Fig. 10 Urbach energy of WO₃:Fe films: (a) films heat-treated for 4 h at 400°C, and (b) films heat-treated for 4 h at 500°C.

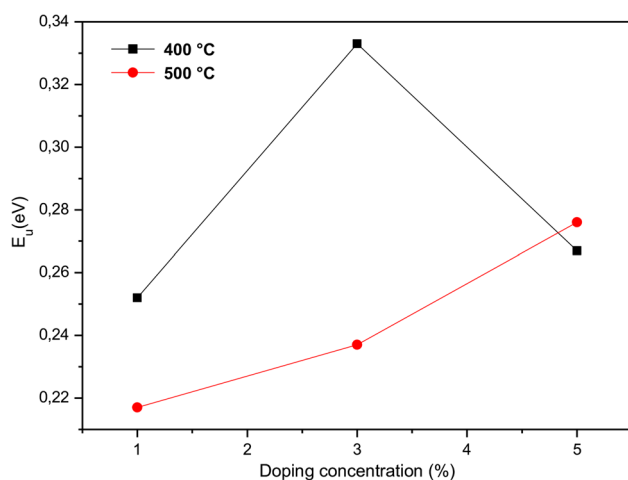


Fig. 11 Variation of the Urbach energy as a function of doping concentration.

increase with increasing temperature of heat treatment. The thermal treatment promotes the growth of the crystallites and enhances the roughness of the surface. All of the $\text{WO}_3\text{:Fe}$ films obtained before thermal treatment are amorphous, whereas those obtained after heat treatment at 400°C and 500°C for 4 h are of polycrystalline nature with a monoclinic structure. Both the stress and the dislocation density increase with Fe-doping in the films heat-treated at 400°C . By contrast, a decrease in the films heat-treated at 500°C is observed. The average crystallite size decreases with Fe-doping while the average particle size increases from 104.3 nm (film doped at 1%) to 327.1 nm (film doped at 3%) and 528.4 nm (film doped at 5%) with Fe-doping.

On the other hand, the films display a good optical transmittance in the visible region sensitive to Fe-doping and thermal treatment. Furthermore, it is observed that E_g^{II} values decrease for both series, while those of E_g^{I} decrease only in the films heat-treated at 500°C . The decrease of the optical band gap with doping is consistent with the introduction of the electronic levels below the conduction band of WO_3 . The width of the tail states in the forbidden region and the Urbach energy (E_u) is sensitive to electronic and structural disorder increases in the films. The above results show that the films prepared in the present study are suitable for application as efficient window material in solar cells, owing to their wider optical transparency.

Acknowledgments The authors wish to thank Professor Bouslama M'Hammed, the Director of the Materials Laboratory (ENPO-Oran), for providing access to AFM measurements, and Dr. Mhamed Guezoul from the same laboratory for his help in these measurements.

Author Contribution All authors contributed to this research work equally.

Funding This work was funded by the Directorate-General for Scientific Research and Technological Development, Ministry of Higher Education and Scientific Research (Algeria).

Conflict of interest The authors declare that they have no conflict of interest.

References

1. P.S. Kolhe, P. Mutadak, N. Maiti, and K.M. Sonawane, *Sens. Actuators A* 304, 111877 (2020).
2. D. Komaraiah, E. Radha, J. Sivakumar, M.R. Reddy, and R. Sayanna, *Opt. Mater.* 108, 110401 (2020).
3. S.K. Muhammad, E.S. Hassan, K.Y. Qader, K.H. Abass, S.S. Chiad, and N.F. Habubi, *Nano Biomed. Eng.* 12, 67 (2020).
4. A.M. Mostafa, and E.A. Mwafy, *J. Mol. Struct.* 1221, 128872 (2020).
5. Q. Wang, H. Fu, J. Ding, C. Yang, and S. Wang, *Opt. Laser Technol.* 125, 106036 (2020).
6. A.K. Mohamedkhair, Q.A. Drmash, M. Qamar, and Z.H. Yamani, *Catalysts* 11, 381 (2021).
7. Y. Kimura, K. Ibano, K. Uehata, I. Hirai, H.T. Lee, and Y. Ueda, *Appl. Surf. Sci.* 532, 147274 (2020).
8. S. Hajirnis, P. Chavan, V. Manapure, A. Patil, A. Khan, B.S. Nadekar, P.S. More, and A.V. Kadam, *Mater. Res. Express* 8, 095503 (2021).
9. F.J. García-García, J. Mosa, A.R. Gonzalez-Elipe, and M. Aparicio, *Electrochim. Acta* 321, 134669 (2019).
10. Y. Zhao, X. Zhang, X. Chen, W. Li, L. Wang, F. Ren, J. Zhao, F. Endres, Y. Li, and A.C.S. Sustain, *Chem. Eng.* 8, 11658 (2020).
11. A. Abareshi, and H. Haratizadeh, *Iran. J. Phys. Res.* 16, 47 (2019).
12. D. Nunes, A.R. Fragoso, T. Freire, M. Matias, A.C. Marques, R.F.D.P. Martins, E. Fortunato, and A. Pimentel, *Phys. Status Solidi - Rapid Res. Lett.* 15, 2100196 (2021).
13. Y.C. Liang, and C.W. Chang, *Coatings* 9, 90 (2019).
14. M. Feng, Y. Liu, Z. Zhao, H. Huang, and Z. Peng, *Mater. Res. Bull.* 109, 168 (2019).
15. J. Juodkazytė, M. Petrulėvičienė, M. Parvin, B. Šebeka, I. Savickaja, V. Pakštis, A. Naujokaitis, J. Virkutis, and A. Gegeckas, *J. Electroanal. Chem.* 871, 114277 (2020).
16. X. San, Y. Lu, G. Wang, D. Meng, X. Gong, and Q. Jin, *Mater. Lett.* 271, 127716 (2020).
17. A. Rydosz, K. Dyndał, K. Kollbek, W. Andrysiewicz, M. Sitarz, and K. Marszałek, *Vacuum* 177, 109378 (2020).
18. N. Matsunami, M. Sataka, and S. Okayasu, *Nucl. Instrum. Methods Phys. Res. B* 460, 185 (2019).
19. L. Pan, Q. Han, Z. Dong, M. Wan, H. Zhu, Y. Li, and Y. Mai, *Electrochim. Acta* 328, 135107 (2019).
20. R. Shakoury, A. Arman, S. Rezaee, A.G. Korpi, S. Kulesza, C. Luna, and M. Mardani, *J. Mater. Sci. Mater. Electron.* 32, 798 (2021).
21. W. Li, X. Zhang, X. Chen, Y. Zhao, L. Wang, M. Chen, Z. Li, J. Zhao, and Y. Li, *Electrochim. Acta* 355, 136817 (2020).
22. Y. Nishijima, K. Enomonoto, S. Okazaki, T. Arakawa, A. Balčytis, and S. Juodkasis, *Appl. Surf. Sci.* 534, 147568 (2020).
23. L. S. Parshina, O. A. Novodvorsky, O. D. Khramova, A. A. Lotin and P. A. Shchur, in *Journal of Physics: Conference Series* **1164**, 012003 (2019).
24. C.M. Chang, Y.C. Chiang, M.H. Cheng, S.H. Lin, W.B. Jian, J.T. Chen, and K. Tsukagoshi, *Sol. Energy Mater. Sol. Cells* 223, 110960 (2021).
25. Z. Han, J. Ren, J. Zhou, S. Zhang, Z. Zhang, L. Yang, and C. Yin, *Int. J. Hydrog. Energy.* 45, 7223 (2020).

26. X. Li, Z. Li, W. He, H. Chen, X. Tang, Y. Chen, and Y. Chen, *Coatings* 11, 959 (2021).
27. G. Mathankumar, P. Bharathi, M.K. Mohan, S. Harish, M. Navaneethan, J. Archana, and C. Muthamizhchelvan, *Mater. Sci. Semicond. Process.* 105, 104732 (2020).
28. V. Saasa, T. Malwela, Y. Lemmer, M. Beukes, and B. Mwakikunga, *Mater. Sci. Semicond. Process.* 117, 105157 (2020).
29. S. Buathet, K. Simalaotao, P. Reunchan, V. Vailikhit, P. Teesetsopon, D. Raknual, and A. Tubtimtae, *Electrochim. Acta* 341, 136049 (2020).
30. M. Arshad, S. Ehtisham-ul-Haque, M. Bilal, N. Ahmad, A. Ahmad, M. Abbas, and M. Iqbal, *Mater. Res. Express* 7, 015407 (2020).
31. H. Khan, M. Habib, A. Khan, and D.C. Boffito, *J. Environ. Chem. Eng.* 8, 104282 (2020).
32. S.S. Hossain, K. Praveena, and P.K. Roy, *J. Mater. Sci. Mater. Electron.* 31, 15097 (2020).
33. M. Kumar Mohanta, T. Kanta Sahu, S. Alam, and M. Qureshi, *Chem. Asian J.* 15, 3886 (2020).
34. C. Qiu, Q. Meng, M. Panchal, C. Li, and B. Wu, *Catal. Commun* 147, 106149 (2020).
35. M. Farooqi, M. Hasan, R. K. Srivastava, in *Proc. Natl. Acad. Sci. India - Phys. Sci.* 90 (2020), pp. 845–859
36. Z. Li, X. Liu, M. Zhou, S. Zhang, S. Cao, G. Lei, C. Lou, and J. Zhang, *J. Hazard. Mater.* 415, 125757 (2021).
37. N. Bashirom, and Q.L. Lee, *Mater. Sci. Forum* 1010, 405 (2020).
38. D. Dong, J. Robichaud, and Y. Djaoued, *Can. J. Chem.* 99, 549 (2021).
39. Y.S. Haiduk, A.A. Khort, M.A. Makhavikou, and A.A. Savitsky, *Mod. Electron. Mater.* 5, 115 (2019).
40. S. M. Abd Al Hussan, N. A. Bakr, A. N. Abd, in *IOP Conference Series: Materials Science and Engineering*, vol. 928 (2020), pp. 072142
41. S. Sivakumar, E. Manikandan, and B. Mahalakshmi, *Vacuum* 173, 109116 (2020).
42. A.A. Akl, I.M. El Radaf, and A.S. Hassanien, *Optik* 227, 165837 (2021).
43. V. Luxmi, and A. Kumar, *Mater. Sci. Semicond. Process.* 104, 104690 (2019).
44. E.M. Ngigi, P.N. Nomngongo, and J.C. Ngila, *Catal. Lett.* 149, 49 (2019).
45. C.T. Nguyen, T.P. Pham, T.L.A. Luu, X.S. Nguyen, T.T. Nguyen, H.L. Nguyen, and D.C. Nguyen, *Ceram. Int.* 46, 8711 (2020).
46. M.M. Thwala, and L.N. Dlamini, *Environ. Technol.* 41, 2277 (2020).
47. S.S. Shendage, V.L. Patil, S.A. Vanalakar, S.P. Patil, J.L. Bhosale, J.H. Kim, P.S. Patil, and Z. Phys. Chem. 234, 1819 (2020).
48. I.A. Rodionov, A.S. Baburin, A.R. Gabidullin, S.S. Maklakov, S. Peters, I.A. Ryzhikov, and A.V. Andriyash, *Sci. Rep.* 9, 1 (2019).
49. L. Xu, G. Zheng, F. Xian, and J. Su, *Mater. Chem. Phys.* 229, 215 (2019).
50. A. Haichour, and N. Hamdadou, *J. Nano- Electron. Phys.* 11, 06020 (2019).
51. L.K. Sharma, M. Kar, R.K. Choubey, and S. Mukherjee, *Chem. Phys. Lett.* 780, 138902 (2021).
52. G. Soman, A. Shajan, J. Jassi, N. K. Vijay, in *AIP Conference Proceedings*, vol. 2263 (2020), p. 050006.
53. P.K. Pothuganti, A. Bhogi, M.R. Kalimi, and P. Reniguntla, *Glass Phys. Chem.* 46, 146–154 (2020).
54. A. Ammari, and M. Trari, *Colloids Surf. A* 61, 178–186 (2019).
55. J. Liu, G. Zhang, K. Guo, D. Guo, M. Shi, H. Ning, T. Qiu, J. Chen, X. Fu, R. Yao, and J. Peng, *Micromachines* 11, 311 (2020).
56. R.I. Eglitis, J. Purans, and R. Jia, *Curr. Comput.-Aided Drug Des.* 11, 455 (2021).
57. D. Acosta, F. Hernández, A. López-Suárez, and C. Magaña, *Solid State Phenom.* 286, 49–63 (2019).
58. S. Kumari, K. Singh, P. Singh, S. Kumar, and A. Thakur, *SN Appl. Sci.* 2, 1 (2020).
59. T. Hamai, S. Inoue, S. Arai, and T. Hasegawa, *Phys. Rev. Mater.* 4, 074601 (2020).
60. A. Ammari, M. Trari, and N. Zebbar, *Mater. Sci. Semicond. Process.* 89, 97–104 (2019).

Publisher's Note Springer Nature remains neutral with regard to jurisdictional claims in published maps and institutional affiliations.